



# Ultrathin $\text{ZnIn}_2\text{S}_4$ nanosheets decorating PPy nanotubes toward simultaneous photocatalytic $\text{H}_2$ production and 1,4-benzenedimethanol valorization

Xinxin Peng<sup>a,b,1</sup>, Junwei Li<sup>a,1</sup>, Luocai Yi<sup>a</sup>, Xi Liu<sup>a,b</sup>, Junxiang Chen<sup>a</sup>, Pingwei Cai<sup>a</sup>, Zhenhai Wen<sup>a,\*</sup>

<sup>a</sup> CAS Key Laboratory of Design and Assembly of Functional Nanostructures, Fujian Provincial Key Laboratory of Nanomaterials, Fujian Institute of Research on the Structure of Matter, Chinese Academy of Sciences, Fuzhou 350002, PR China

<sup>b</sup> University of Chinese Academy of Science, Beijing 100049, PR China

## ARTICLE INFO

### Keywords:

Photocatalysis  
 $\text{H}_2$  production  
 $\text{ZnIn}_2\text{S}_4$  nanosheets  
 1,4-Benzenedimethanol upgrading

## ABSTRACT

It is highly desirable to make full use of photogenerated charge carriers by elaborately designing high-efficiency multifunctional photocatalysts with achieving bi-value-added production. Herein, we report the photocatalyst with ultrathin  $\text{ZnIn}_2\text{S}_4$  nanosheets decorating polypyrrole nanotubes, thanks to the matched bandgap, is capable of harvesting visible light for photocatalysis, during which the photoexcited electrons and holes are used for  $\text{H}_2$  evolution and 1,4-benzenedimethanol (BDM) upgrading oxidation, respectively. Comprehensive experiments and density functional theory calculations indicate that the photoinduced electrons tend to be transferred to the inner PPy nanotubes of PPy@ZIS composite for photocatalytic  $\text{H}_2$  generation, while the photoexcited holes favorably oxidize BDM into 1,4-phthalaldehyde (PAD) on outer ZIS nanosheets of PPy@ZIS composite. The optimized PPy@ZIS exhibits an apparent quantum efficiency of 6.43% (at 420 nm) for photocatalytic  $\text{H}_2$  evolution and BDM valorization into PAD at a rate of  $735 \mu\text{mol g}^{-1} \text{h}^{-1}$ , remarkably promoting the utilization efficiency of charge carriers.

## 1. Introduction

Converting solar energy directly into fuels or value-added chemicals has been envisaged as a promising route for sustainable development [1]. Of them, solar-driven hydrogen ( $\text{H}_2$ ) has attracted tremendous attention since  $\text{H}_2$  has been generally recognized as one of the cleanest energies. To this end, high-efficiency photocatalysts should be developed for the decomposition of water to produce  $\text{H}_2$  [2], which has become a promising alternative to fossil fuels [3]. However, the overall water splitting is highly limited by the half-reaction of slow water oxidation. While most researches are devoted to exploring efficient photocatalysts for  $\text{H}_2$  production accompanying with consuming the hole using sacrifice [4], such as ascorbic acid (AA), and triethanolamine (TEOA), etc. Little research throws on how to simultaneously efficiently utilize the photoexcited charge carriers [5]. In order to make full use of both photoinduced electrons and holes, an alternative oxidation reaction to either water oxidation or sacrifices oxidation should be designed,

in this manner can  $\text{H}_2$  and value-added chemicals be simultaneously generated [6,7].

Oxidation of some organics represents an interesting direction for the synthesis of value-added chemicals, including C-H functionalization [8,9], C-N coupling [10,11], alcohol oxidation [12,13], biomass oxidation [14,15], and so on. Normally, aldehydes are considered to have strategic significance, because they are important raw materials or intermediates in organic synthesis and fine chemical industries and are widely used for complex syntheses in the confectionery fragrance, pharmaceutical [16,17]. It is worth mentioning that selective conversion of alcohols is an effective way to gain high-value aldehydes. Traditionally, transforming alcohols into aldehydes requires either toxic oxidants or expensive noble metals catalysts, which are not conducive to sustainable development [18]. Selective photocatalytic oxidation of alcohols is an effective strategy to prepare high value-added aldehydes with the advantages of environmentally friendly and low cost [19,20]. Typically, the photocatalytic transformation of alcohols into aldehydes occurs in organic

\* Corresponding author.

E-mail address: [wen@fjirsm.ac.cn](mailto:wen@fjirsm.ac.cn) (Z. Wen).

<sup>1</sup> These authors contributed equally to this work.

solvents with oxygen as an electron acceptor [21]. By contrast, coupling photocatalytic alcohol oxidation with  $H_2$  evolution (water as an electron acceptor) can potentially produce dual valuable products, i.e., aldehyde and  $H_2$ , promising for the solar-to-chemical future [22,23]. Nevertheless, there have been many works on this topic, but how to design and develop high-performance photocatalysts that match well for photocatalytic  $H_2$  generation and selective alcohol oxidation is still facing daunting challenges, especially the preparation of high value-added and multifunctional group products through this method. Among them, the photocatalytic oxidation of 1,4-benzenedimethanol (BDM) to prepare 1,4-phthalaldehyde (PAD) is representative and has little research.

Indium zinc sulfide  $ZnIn_2S_4$  (ZIS) has exhibited great potentials in photocatalytic  $H_2$  production and selective organic oxidation due to its matched visible light absorption band structure and excellent chemical stability [24], but facile recombination of photoexcited charge carriers significantly decreases the photocatalytic efficiency. Therefore, various strategies have been proposed to improve the photocatalytic performance of ZIS [25,26]. Nevertheless, there remains great space in further advancing the performance of the ZIS-based photocatalyst by facilitating the mass transmission and enhancing the separation of charge carriers [27,28]. The conducting polymer of polypyrrole (PPy), thanks to its favorable characteristics of nontoxicity, facile synthesis, good conductivity, has been widely used as the photoinduced charge carrier collectors of semiconductors, which can improve charge separation by microstructural modulation [29,30].

In this work, we report a two-step process for *in-situ* growth of ultrathin ZIS nanosheets on PPy nanotubes with the formation of PPy@ $ZnIn_2S_4$  composite, which presents highly desirable photocatalytic properties for simultaneous generation of  $H_2$  and PAD via water reduction and BDM selective oxidation, respectively, as demonstrated by an apparent quantum efficiency (AQE) of 6.43% (at 420 nm) for photocatalytic  $H_2$  production and BDM conversion selectivity of 98.9%.

## 2. Experimental section

### 2.1. Synthesis of PPy

All chemicals used are analytical-grade reagents without further purification. 0.480 g of methyl orange was dispersed in 300 mL of deionized (DI) water under stirring, then 2.34 g of  $FeCl_3$  was added into the solution. Afterward, 1000  $\mu$ L of pyrrole (Py) was added and stirred for 24 h at room temperature. The black product was separated and washed by suction filtration with DI water and ethanol several times until the filtrate is colorless. Finally, polypyrrole (PPy) was collected after drying under vacuum at 60 °C for 24 h in an oven.

### 2.2. Synthesis of PPy@ZIS

20.0 mg of PPy was dispersed in 40 mL of dilute HCl solution (0.01 M) and sonicated for 15 min, then transferred the above solution to a glass bottle. 10 mL of glycerol was added into the solution and stirred for 15 min. Next, 180.4 mg of  $In(NO_3)_3 \cdot xH_2O$ , 140.6 mg of  $Zn(NO_3)_2 \cdot 6H_2O$ , and 142.2 mg of thioacetamide (TAA) were successively added into the above solution. After stirring for 30 min, the solution was put into an oil bath and continuously stirred at 80 °C for 2 h. The product was washed with ethanol and DI water, then dried at 60 °C, the obtained product was denoted as 10%-PPy@ZIS, where the theoretical weight ratio of PPy:  $ZnIn_2S_4$  is 10%. On this basis, 5%-PPy@ZIS and 20%-PPy@ZIS products were synthesized as the same procedure except for adding different amounts of ingredients.

### 2.3. Synthesis of ZIS and PPy&ZIS

ZIS was synthesized as the same reaction procedure of PPy@ZIS except without adding PPy. 20.0 mg of PPy and 200 mg of ZIS were dispersed in 100 mL of dilute HCl solution (0.01 M) and sonicated for 30

min, the products were washed and dried, denoted as PPy&ZIS.

### 2.4. Photoelectrochemical characterization

All the photoelectrochemical measurements were monitored by a CHI 760E electrochemical work station (Shanghai Chenhua, China) with a three-electrode system under visible light irradiation. The working electrode was prepared by using samples coated on indium-tin oxide (ITO) glass with an area of 1  $cm^2$ . An Ag/AgCl electrode and a graphite rod were used as reference electrode and counter electrode, respectively. The photoelectrochemical experiments were tested in an argon stream deoxy sodium sulfate electrolyte (0.2 M).

### 2.5. Coupling of photocatalytic $H_2$ evolution and 1,4-benzenedimethanol oxidation

Typically, 20.0 mg of each photocatalyst was dispersed in 100 mL of 1,4-benzenedimethanol aqueous solution (0.01 M), then sonicated for 15 min. Prior to the photocatalytic reaction, the photocatalytic reaction system was degassed under vacuum until the pressure was stable. A 300 W Xenon lamp (PLS-SXE 300, Beijing Perfect light Co., Ltd) with a 420 nm cutoff filter was employed as the visible light source. The system was stirred by a magnetic stirrer at 25 °C by injecting constant temperature water, and the  $H_2$  was monitored by an online gas chromatograph (GC-2014, Ar carrier) equipped with a 5 Å molecular sieve and a TCD detector. The structure of the liquid product was characterized by a nuclear magnetic resonance (NMR) spectrometer. Deuterium oxide ( $D_2O$ ) was used as lock solution and dimethyl sulfoxide (DMSO) as an internal standard. The photocatalytic activity test of 10%-PPy@ZIS on different substrates ensured that the molar amount of alcoholic hydroxyl groups was the same as that of the BDM test. The apparent quantum efficiency (AQE) for  $H_2$  production was obtained under the Xenon lamp equipped with different single-wavelength filters (400, 420 and 450 nm), and the average spectral irradiance of 100  $mW\ cm^{-2}$ . The AQE was evaluated by the following equation:

$$AQE = \frac{2 \times N(H_2)}{N(Photons)} = \frac{2 \times h \times c \times n(H_2) \times N_A}{\lambda \times P \times t \times S}$$

where the  $N(H_2)$  is the number of evolved hydrogen molecules,  $N(Photons)$  is the number of incident photons,  $h$  is the Planck constant,  $c$  is the light speed,  $n(H_2)$  is the molar amount of hydrogen evolution,  $N_A$  is the Avogadro constant,  $\lambda$  is the wavelength of monochromatic light,  $P$  refers to the average spectral irradiance,  $t$  is the irradiation time, and  $S$  is the irradiation area.

## 3. Results and discussion

### 3.1. Synthesis and characterization

Fig. 1a shows the synthesis of the PPy@ $ZnIn_2S_4$  (PPy@ZIS) composite that mainly includes two steps. The polypyrrole (PPy) is firstly prepared via a simple chemical oxidative polymerization method, followed by the *in-situ* growth of ZIS on PPy nanotubes via a hydrothermal process. For comparison study, the PPy@ZIS with different mass ratios, the pure ZIS without PPy nanotubes as the supports, and the mechanical mixture of PPy nanotubes and ZIS (PPy&ZIS) were prepared. The field emission scanning electron microscopy (FESEM) image (Fig. 1b) of PPy exhibits uniform one-dimensional (1D) nanotubes with an average diameter of about 300 nm. Notably, the pure ZIS without PPy supports show microsphere morphology comprising interwoven two-dimensional (2D) nanosheets (Fig. 1c). As disclosed in Fig. 1d, the 10%-PPy@ZIS composites show that the ZIS nanosheets are uniformly growing and covering on the surfaces of PPy nanotubes. The transmission electron microscopy (TEM) images of 10%-PPy@ZIS (Fig. 1e, f) reveal that the 1D PPy nanotubes are encapsulated by ultrathin and staggered 2D ZIS

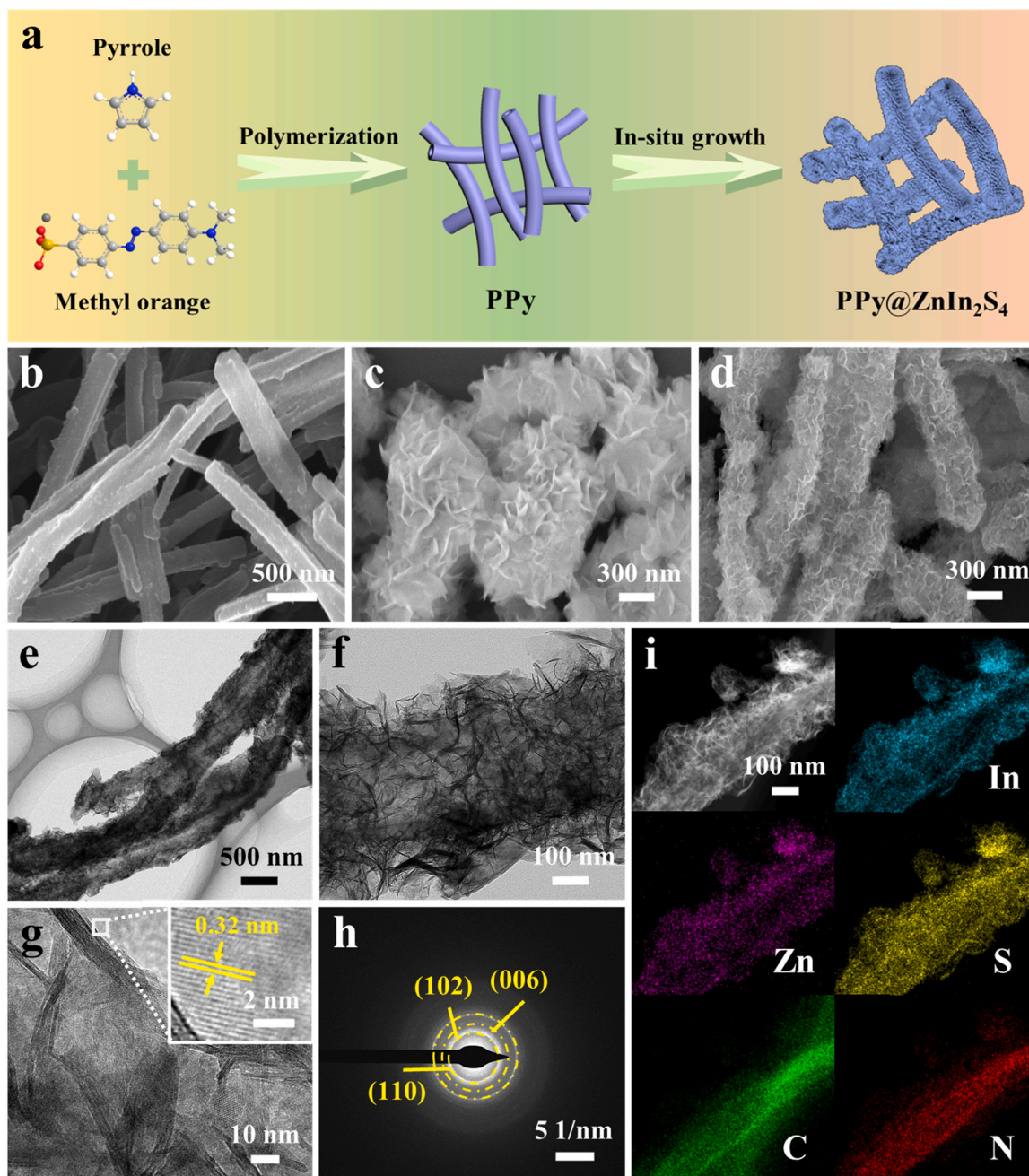


**Fig. 1.** (a) Schematic preparation of PPy@ZnIn<sub>2</sub>S<sub>4</sub>. FESEM images of (b) PPy, (c) ZIS, and (d) 10%-PPy@ZIS. (e, f) TEM images, (g) HRTEM image, (h) SAED pattern and (i) Elemental mapping images of 10%-PPy@ZIS.

nanosheets. As displayed in Fig. 1g, the high-resolution TEM (HRTEM) image of 10%-PPy@ZIS shows clear lattice fringes of 0.32 nm, which is indexed to the (102) crystal plane of hexagonal ZIS [31]. The selected area electron diffraction (SAED) pattern (Fig. 1h) also further confirms the existence of ZIS in 10%-PPy@ZIS.

The time-dependent structural evolution of 10%-PPy@ZIS was monitored by FESEM (Fig. S1), revealing the ZIS nanosheets were gradually grown on PPy nanotubes surface. In addition, the mass ratio of PPy to ZIS in the PPy@ZIS composites can be controlled by adjusting PPy and the precursors of ZIS. The 20%-PPy@ZIS shows sparse ZIS nanosheets growing on PPy nanotubes due to the less amount of ZIS (Fig. S2), while the 5%-PPy@ZIS presents crowded ZIS nanosheets on PPy nanotubes due to the excess amount of ZIS (Fig. S3). The 10%-PPy@ZIS composite displays a rather uniform and compact composite structure, where the ZIS nanosheet can well contact with the PPy

nanotube, which will facilitate the rapid migration and separation of photoexcited electrons and holes during the photocatalytic reaction. The FESEM image of PPy@ZIS (Fig. S4) shows that PPy nanotubes are not covered by ZIS nanosheets and mix with the microspheres assembled from ZIS nanosheets. The elemental mapping of the 10%-PPy@ZIS shows that C and N elements are distributed inner of the sample, while Zn, In and S are distributed outer of 10%-PPy@ZIS composite, which is in accordance with the results as discussed above.

Fig. 2a shows UV-Vis diffuse reflectance spectra (DRS), which reveals that the edge absorption of ZIS appears at around 500 nm, corresponding to its intrinsic bandgap [32]. The edge absorption gradually increased with the increasing amount of PPy in PPy@ZIS, and the absorption in the region of visible light gradually enhanced, resulting in more photoexcited charge carriers [33]. Due to the strong light absorption of the black PPy, the bandgap cannot be accurately calculated



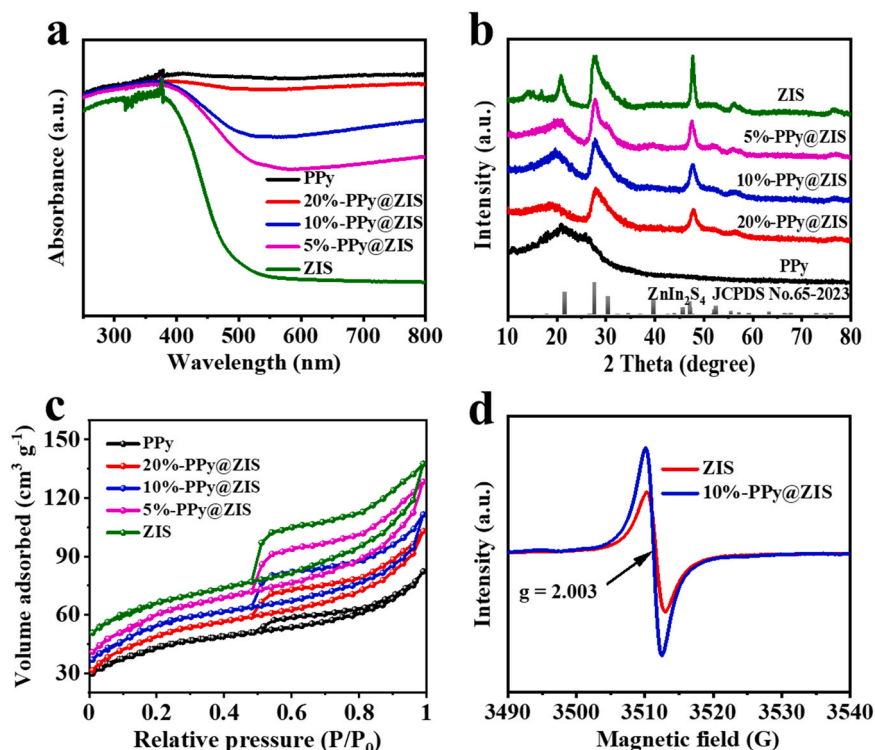


Fig. 2. (a) UV-Vis DRS spectra, (b) XRD pattern, and (c) Nitrogen adsorption-desorption isotherms of PPy, PPy@ZIS and ZIS. (d) EPR spectra of 10%-PPy@ZIS and ZIS.

by the UV-Vis DRS method [34]. The crystal structure was examined by X-ray diffraction (XRD), as depicted in Fig. 2b. The PPy shows a broad XRD peak at 25.8° due to its amorphous structure. The set of PPy@ZIS composites show the typical diffraction peaks of hexagonal ZIS and the intensities decreased with increasing the content of PPy. The pure ZIS shows five XRD peaks at 21.8°, 27.9°, 47.0°, 52.3° and 55.6°, which are attributed to the hexagonal ZIS (JCPDS No. 65-2023) [35]. Fig. 2c shows the nitrogen adsorption-desorption isotherms of the set of samples, they show type IV isotherm and H<sub>3</sub>-type hysteresis loops, implying the formation of mesopores [36]. The Brunauer-Emmett-Teller (BET) specific surface area of the set of samples is shown in Table S1. The specific surface areas of the PPy@ZIS composites increase with increasing the content of ZIS, which are assigned to the high surface area of PPy nanotubes and ZIS nanosheets hierarchical structure. The PPy@ZIS composites can provide more active sites, which is beneficial to improve photocatalytic performance. Although ZIS displays the highest specific surface area, which doesn't mean that it will have the highest photocatalytic performance, because the photocatalytic activity is also connected with the charge transfer and separation.

As can be seen in Fig. S5, the Fourier transfer infrared (FT-IR) spectrum of PPy exhibits several typical peaks, the peaks at 788 cm<sup>-1</sup> and 957 cm<sup>-1</sup> are ascribed to C-H wagging vibration and ring deformation, while the peaks at 1042 cm<sup>-1</sup> and 1300 cm<sup>-1</sup> are related to C-H stretching and =C-H plane bending [37]. And the other three peaks at 1421 cm<sup>-1</sup>, 1550 cm<sup>-1</sup> and 1654 cm<sup>-1</sup> are due to C-H in-plane, C=C symmetric and C-N stretching, respectively [38]. The FT-IR spectrum of the PPy@ZIS composite maintains the characteristic peaks of PPy. The typical peaks at 1420 cm<sup>-1</sup> and 1100 cm<sup>-1</sup> can be indexed to Zn-S and In-S vibrational mode of ZIS, respectively [39]. Fig. 2d displays the electron paramagnetic resonance (EPR) of ZIS and 10%-PPy@ZIS. ZIS presents a sharp signal at 3512 G (g value is 2.003), suggesting the existence of S vacancies (Vs) [40]. The 10%-PPy@ZIS composite shows a stronger peak intensity than ZIS, which means that the ZIS nanosheets grown on PPy nanotubes inclines to enhance the S vacancies. It is worth mentioning that the EPR signal intensity increases with the increase of

the visible light irradiation time, indicating that S vacancies also increase (Fig. S6), which may be beneficial to the photocatalytic activity.

X-ray photoelectron spectroscopy (XPS) was used to study the surface properties and chemical state of the samples (Fig. 3 and Fig. S7). As displayed in Fig. 3a, the survey XPS spectrum indicates that 10%-PPy@ZIS composites consist of C, N, S, In, and Zn elements, which are consistent with elemental mapping (Fig. 1i). As disclosed in Fig. 3b, the high-resolution Zn 2p spectrum of 10%-PPy@ZIS composite can be fitted into two peaks at 1021.3 and 1044.4 eV, which are ascribed to the Zn 2p<sub>3/2</sub> and Zn 2p<sub>1/2</sub>, respectively [35]. Fig. 3c shows the high-resolution In 3d spectrum with two peaks at 452.3 and 444.2 eV that can be attributed to In 3d<sub>3/2</sub> and In 3d<sub>5/2</sub>, respectively, implying the existence of In<sup>3+</sup> cation in 10%-PPy@ZIS [41]. As can be seen in Fig. 3d, the high-resolution S 2p spectrum of ZIS displays two peaks at 161.9 and 160.8 eV, ascribing to S<sup>2-</sup> anion [42]. The S 2p spectrum of 10%-PPy@ZIS shows two peaks at 162.3 and 161.2 eV, which has an obvious positive shift in the binding energies and slight decrease in the intensity of S 2p compared with ZIS, meaning that there is an interaction between PPy and ZIS in 10%-PPy@ZIS composite to affect the electron transfer [43]. The intensity ratio of S 2p to In 3d and Zn 2p in 10%-PPy@ZIS composite is smaller than that of ZIS, further verifying the existence of S vacancies [28,44]. The Zn 2p spectrum is fitted into two peaks at 1021.5 and 1044.6 eV in ZIS, and the In 3d spectrum shows two peaks at 444.5 and 452.3 eV, which is similar to the reported ZIS [45]. The binding energies of In 3d and Zn 3d for 10%-PPy@ZIS composite are higher than those of ZIS, which could be rationally assigned to the interaction between the PPy and ZIS. The peak position distance of In 3d and Zn 3d in 10%-PPy@ZIS composite is significantly reduced, indicating that the existence of S vacancies [34,43]. The high-resolution C 1s spectra of PPy display three peaks (Fig. 3e and Table S2) at 284.8 eV (C-C/C=C), 286.0 eV (C-N) and 287.8 eV (N=C-N) [46], the high binding energy of C-N bond is positive shift in the PPy@ZIS composite compare with PPy. Fig. 3f presents the high-resolution N 1s spectra of PPy, which is deconvoluted into three species located at 401.5 eV (C-NH), 400.1 eV (N-H), and 399.1 eV (C-N=C) [47]. The

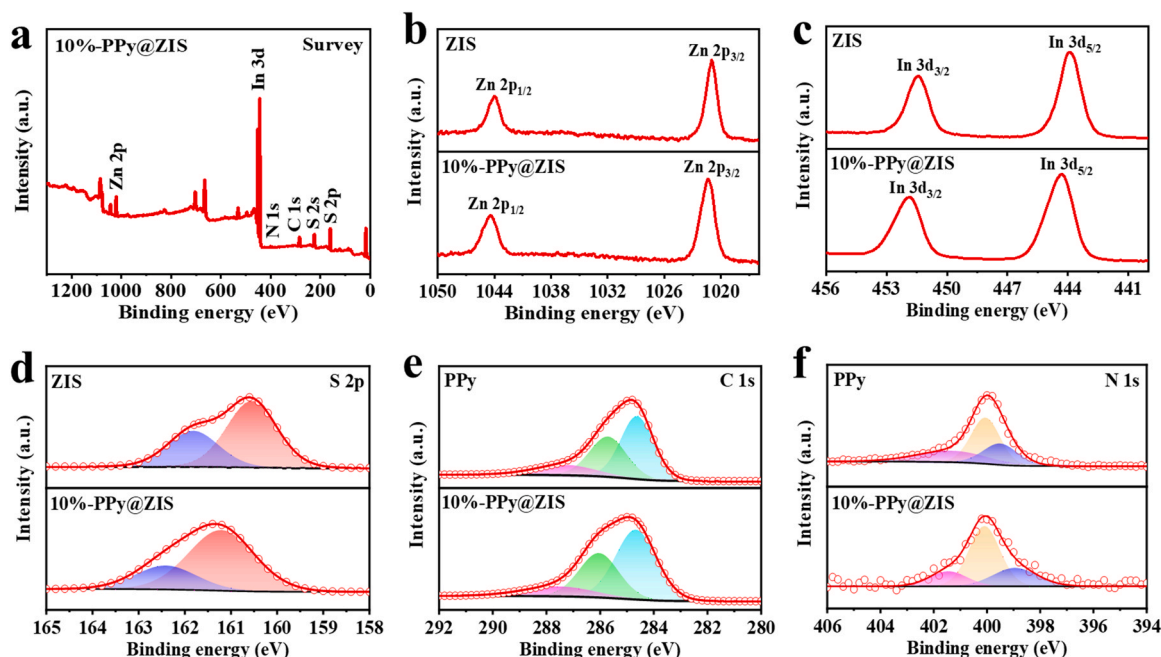


**Fig. 3.** (a) XPS survey spectra of 10%-PPy@ZIS. XPS high-resolution spectra (b) Zn 2p, (c) In 3d and (d) S 2p for ZIS and 10%-PPy@ZIS, respectively. XPS high-resolution spectra of (e) C 1s and (f) N 1s for PPy and 10%-PPy@ZIS, respectively.

10%-PPy@ZIS composite manifests an increased peak intensity of N-H and negative shift for C-N=C peak (Table S3), which is attributed to the interaction between the PPy and ZIS in 10%-PPy@ZIS composite. Based on the above results, it is proved that there is the strong interaction between PPy and ZIS in the 10%-PPy@ZIS composite leads to the increased amount of S vacancies.

### 3.2. Photocatalytic activity

The photocatalytic performance was evaluated in 0.01 M 1,4-

benzenedimethanol (BDM) aqueous solution under visible light irradiation. For PPy, there is almost no H<sub>2</sub> and 1,4-phthalaldehyde (PAD) production (Fig. 4a), implying the pure PPy is inactive, while the pure ZIS behave an improved photocatalytic activity toward H<sub>2</sub> evolution and PAD production with a production rate of 367 and 190  $\mu\text{mol g}^{-1} \text{h}^{-1}$ , respectively. Notably, the photocatalytic performance of PPy@ZIS composites is significantly enhanced. In particular, the 10%-PPy@ZIS composite displays the highest photocatalytic H<sub>2</sub> evolution of 1428  $\mu\text{mol g}^{-1} \text{h}^{-1}$ , which is 3.90 times higher than that of pure ZIS, meaning that PPy could significantly promote the utilization of solar

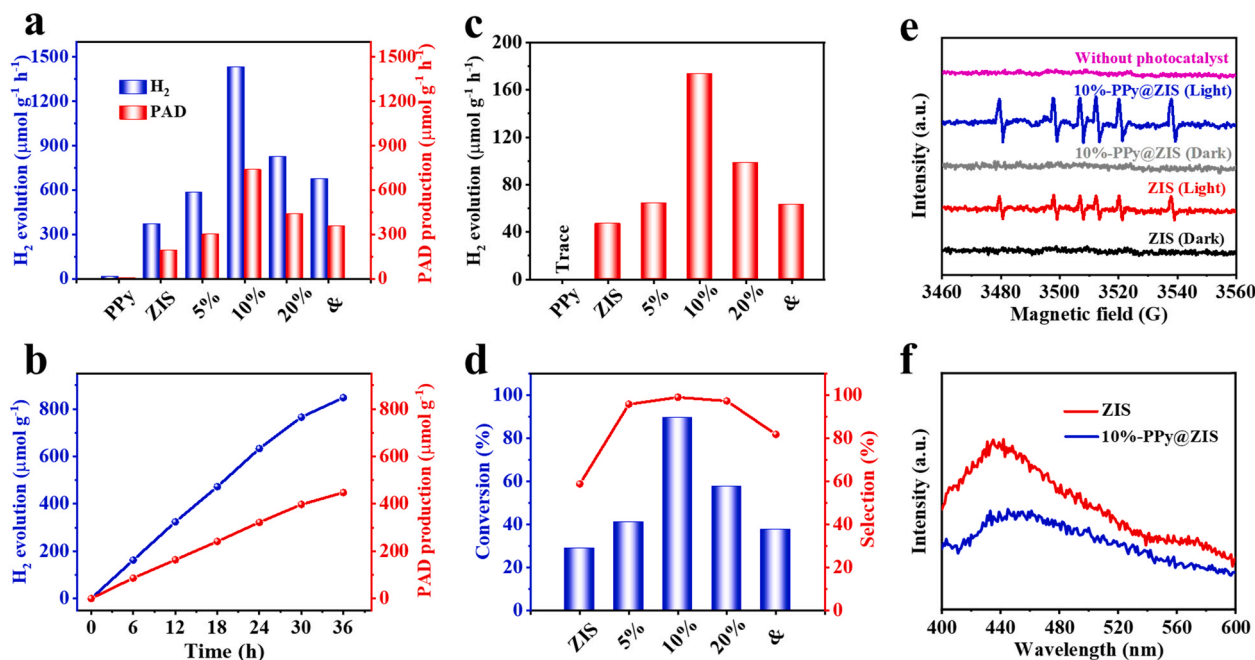


**Fig. 4.** (a) Photocatalytic H<sub>2</sub> evolution and PAD production efficiency, and (b) Time course of H<sub>2</sub> evolution and PAD production for 10%-PPy@ZIS. (c) Photocatalytic H<sub>2</sub> evolution in pure water. (d) Conversion and selection of PAD production after 36 h. (e) DMPO spin-trapping EPR spectra of 10%-PPy@ZIS and ZIS in BDM water solution with or without visible light irradiation. (f) PL spectra of ZIS and 10%-PPy@ZIS.

energy and enhance photocatalytic activity. The 10%-PPy@ZIS composite shows a relatively high apparent quantum efficiency (AQE) for photocatalytic  $\text{H}_2$  production of 6.43% at 420 nm (Fig. S8 and Table S4&5). Compared with commonly used sacrificial agents, the photocatalytic hydrogen production performance of BDM as a hole sacrificial agent is only slightly inferior (Fig. S9). The photocatalytic PAD production rate is consistent with the performance of  $\text{H}_2$  evolution, the 10%-PPy@ZIS composite displays the highest photocatalytic PAD production ( $735 \mu\text{mol g}^{-1} \text{h}^{-1}$ ), which is 3.87 times higher than that of pure ZIS. The 20%-PPy@ZIS and 5%-PPy@ZIS composites have inferior activity than that of the 10%-PPy@ZIS composite, in which the former has fewer interactions between PPy and ZIS, while the latter may be ascribed to the formation of ZIS microspheres on PPy lead to insufficient utilization. The photocatalytic activity of PPy&ZIS is also tested, which is lower than 10%-PPy@ZIS composite, proving that PPy@ZIS composite structure can efficiently promote photocatalytic activity, and its essence is to promote the separation efficiency of photoinduced charge carriers. It is worth mentioning that the ratio of the  $\text{H}_2$  evolution rate to the PAD production rate of all samples is close to 2:1. As shown in Fig. S10, with the amount of ZIS gradually increasing, the optimal rate of 10%-PPy@ZIS also appears plateau regions. The relatively large amount of the composite material will increase scattering and weaken penetration depth of incident light, thereby weakening the excitation of ZIS in PPy@ZIS. In a nutshell, the 10%-PPy@ZIS composite shows excellent photocatalytic performance, which is a result of the synergetic contribution of ultrathin ZIS nanosheets on PPy nanotubes and the composite structure between PPy and ZIS.

The durability test of the 10%-PPy@ZIS composite was evaluated by measuring the long-term photocatalytic  $\text{H}_2$  and PAD production. As displayed in Fig. 4b, the photocatalytic activity of 10%-PPy@ZIS composite shows a linearly increased production rate for both  $\text{H}_2$  and PAD within 24 h continuous running, they tend to decrease slightly after 20 h running majorly due to gradual consumption of BDM and the corrosion of photocatalyst. After photocatalytic reaction 36 h, the XRD intensity of 10%-PPy@ZIS had a certain degree of decline after the long-term test, the characteristic peaks at each position were still intact (Fig. S11a), indicating that its crystal structure is basically maintained. However, it can be found from the SEM image that the morphology of 10%-PPy@ZIS after the test has indeed a certain degree of change, which shows that there is a certain amount of corrosion during the long-term test (Fig. S11b). In order to explore the role of BDM, the photocatalytic activity of  $\text{H}_2$  production in pure water was also studied, as shown in Fig. 4c. Even for the 10%-PPy@ZIS, which performs best with an  $\text{H}_2$  evolution rate of  $173.3 \mu\text{mol g}^{-1} \text{h}^{-1}$ , this value is remarkably lower than that in the presence of BDM, implying that BDM can effectively promote the production of  $\text{H}_2$ . As shown in Fig. 4d, 10%-PPy@ZIS composite exhibits the highest efficiency toward BDM oxidation conversion into PAD production with the selectivity of 98.9% (Fig. S12). As shown in Fig. S13, we detected the presence of corresponding by-products, so the reaction formula of the potential products for BDM oxidation was shown in Fig. S14. The chemical precipitation method was also used to detect the product PAD [48]. As disclosed in Table S6, the results are close to those obtained by NMR, suggesting that this method is feasible. The sediment product can be verified by some characterization (Fig. S15–20). Importantly, the simultaneous photocatalytic  $\text{H}_2$  generation and selective BDM oxidation reactions on 10%-PPy@ZIS indicates that both the electrons and holes produced by the photoexcitation can be efficiently used to convert solar energy into value-added chemicals. As shown in Table S7, the 10%-PPy@ZIS composite can also be used for the oxidation of other alcohols and exhibits good photocatalytic performance.

### 3.3. Mechanism analysis

To reveal the photocatalytic reaction process, some contrast experiments were performed. As shown in Table S8, either in the absence of

photocatalysts or in dark, the photocatalytic reaction of BDM oxidation and  $\text{H}_2$  production hardly proceeds, which means that the photoredox reaction is a light-driven process. When deionized water is replaced by acetonitrile, photocatalytic  $\text{H}_2$  evolution decreases dramatically, implying that hydrogen mainly comes from water, and the  $^2\text{D}$  isotope labeling experiments also proved it (Table S9). The photocatalyst could not catalyze the decomposition of deuterium water ( $\text{D}_2\text{O}$ ) into deuterium ( $\text{D}_2$ ), because the atomic mass of deuterium is heavier, which reduces its chemical reactivity [49–51]. To further explore the possible mechanism, several quenching tests with the addition of some scavengers were performed to verify the active species. As disclosed in Fig. S21, when the sodium sulfite as hole scavenger or the sodium bromate as electron scavenger is added into the reaction system, the photocatalytic production of PAD or  $\text{H}_2$  decreased, suggesting both photoexcited holes and electrons are consumed in the photoredox reaction. Additionally, the addition of 5,5-dimethyl-1-pyrrole-N-oxide (DMPO), a carbon-centered free radical scavenger [52], shows the apparent adverse influence of PAD production, which means that carbon-centered free radical may be the active species in the photocatalytic oxidation reaction. It is worth mentioning that the addition of tert-butanol shows the negligible influence on PAD production, which means that hydroxyl radical is not the active species. To obtain more clues about the mechanism of radical intermediates, the EPR technique using DMPO as the capture reagent was utilized [28,51]. As shown in Fig. 4e, there is no signal in dark. And there is no corresponding EPR signal in the absence of photocatalyst, which can eliminate the interference of substrate and capture reagent. Nevertheless, 10%-PPy@ZIS composite appears a CH(OH)Ph-DMPO signal at a g value of 2.006 under visible light irradiation, implying the production of  $^*\text{CH}(\text{OH})\text{Ph}$  radicals [53]. The signal of CH(OH)Ph-DMPO is also obtained on pure ZIS, but the EPR signal intensity is weaker than that of 10%-PPy@ZIS, which is consistent with the photocatalytic activity.

To further obtain relevant information about the recombination of charge carriers, the photoluminescence (PL) spectrum was performed under 365 nm excitation light. As displayed in Fig. 4f, the pure ZIS shows an emission peak near 442 nm. The emission peak of 10%-PPy@ZIS composite is similar to pure ZIS, whereas the fluorescence intensity is significantly reduced, indicating that there is a recombination of fewer photoexcited carriers, which is beneficial to photocatalysis. The transient photocurrent of ZIS displays a lower response density than that of PPy@ZIS composite (Fig. S22a), confirming that PPy in the PPy@ZIS composite can enhance the separation and inhibit the recombination of photogenerated charge carriers, as well as electrochemical impedance spectroscopy (EIS) is further conducted to confirm it. As disclosed in Fig. S22b, the PPy@ZIS composite has a smaller EIS arc radius than that of pure ZIS, suggesting that PPy can enhance the transfer efficiency of photoexcited charge carriers, and further improving photocatalytic activity. Additionally, the bandgap structure of ZIS is shown in Fig. S23. In a word, the content of PPy affects the photocatalytic performance, the fluorescence and impedance results are consistent with it.

Density functional theory (DFT) calculations were employed to acquire an atomic insight into the BDM oxidation reaction performance of PPy@ZIS. According to the above analysis, the 10%-PPy@ZIS composite had more sulfur vacancies than ZIS, so we introduced ZIS with sulfur vacancies ( $\text{ZIS}_{\text{Vs}}$ ). The BDM oxidation reaction contains several possible paths, driven by the different energy required for the dehydrogenation process on the C-H bond and the O-H bond, also, the path with minimum Gibbs free energy is selected as the optimal path. To screen out the best path for BDM oxidation reaction on the ZIS and  $\text{ZIS}_{\text{Vs}}$ , we analyze four possible paths in BDM oxidation reaction process from BDM oxidation reaction to PAD (Fig. S24 and Fig. S25). Subsequently, we calculate Gibbs free energy of the all-possible reaction for BDM oxidation reaction process on the ZIS and  $\text{ZIS}_{\text{Vs}}$  (Fig. 5a, b and Fig. S26–28). Meanwhile, the best path (Path 4) of BDM oxidation reaction on both materials are identified in both free energy diagram, in which path, the energy barrier

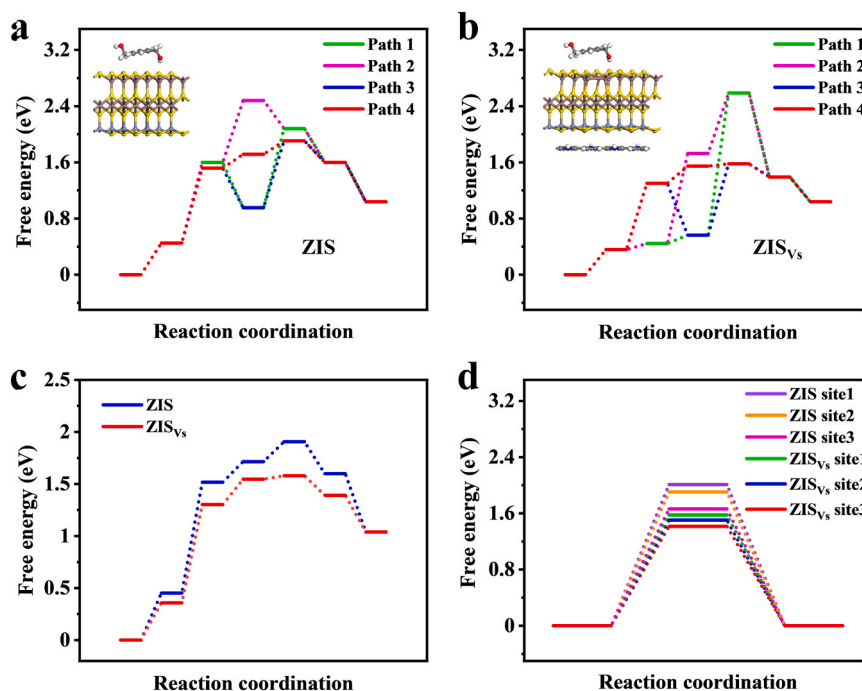


**Fig. 5.** The free energy diagrams of 4 pathways in (a) ZIS and (b)  $\text{ZIS}_{\text{Vs}}$ . (c) The free energy profiles with the lowest energy barrier of ZIS and  $\text{ZIS}_{\text{Vs}}$  are presented by blue and red lines respectively. (d) The free energy profiles for hydrogen adsorption at different active sites of ZIS and  $\text{ZIS}_{\text{Vs}}$ .

of the rate-determining step (RDS) is lower than that of other paths, indicating the Path 4 is the most likely reaction path. Additionally, the RDS of BDM oxidation reaction is the detachment process of the first H atom on C-H bond, suggesting the energy required for the dehydrogenation process on the C-H bond is lower than that on the O-H bond. As shown in the free-energy diagram (Fig. 5c), the RDS of BDM oxidation reaction on  $\text{ZIS}_{\text{Vs}}$  (0.94 eV) is lower than that on ZIS (1.06 eV), suggesting the  $\text{ZIS}_{\text{Vs}}$  has a better activity for BDM oxidation reaction. Therefore, the introduction of PPy can lead to high performance for BDM oxidation reaction. These results suggesting the introduction of PPy could bring about enhanced BDM oxidation reaction ability in  $\text{ZIS}_{\text{Vs}}$ . On the other hand, in order to evaluate the HER activity of the above materials, the adsorption free energies of H ( $\Delta G_{\text{H}}^*$ ,  $\text{H}^*$  adsorption Gibbs energy) are employed as an effective activity descriptor for HER activity. The more neutral  $\Delta G_{\text{H}}^*$  of a catalyst, the better its catalytic activity. Therefore, the  $\Delta G_{\text{H}}^*$  on different sites of ZIS and  $\text{ZIS}_{\text{Vs}}$  were calculated to evaluate their HER activity (Fig. S29 and Fig. S30). As shown in Fig. 5d, the  $\Delta G_{\text{H}}^*$  at various active sites in the  $\text{ZIS}_{\text{Vs}}$  is more neutral than ZIS, suggesting these active sites of  $\text{ZIS}_{\text{Vs}}$  have better activity for HER than all active sites of ZIS. Therefore, the introduction of PPy in ZIS can also contribute to the advanced HER activity. According to the above analysis, the introduction of PPy in ZIS can lead to high performance for BDM oxidation reaction and HER process.

Based on the above analysis, a tentative mechanism can be proposed for simultaneous photocatalytic  $\text{H}_2$  evolution and BDM oxidation on PPy@ZIS composite (Fig. 6 and Fig. S31). Under visible light irradiation, the ZIS in PPy@ZIS composite is excited to produce electrons and holes, the electrons on the conduction band of ZIS could quickly transfer to the PPy, and then combine with protons from water to generate  $\text{H}_2$ . The photoexcited holes on the valence band of ZIS can be consumed by BDM, while the proton of the OH group in BDM is adsorbed on the surface of ZIS, and another proton of C-H adsorbed on S vacancy, generating dissociative protons and carbon-centered radical, then the latter is oxidized by holes to obtain aldehyde. According to the above steps, the two hydroxymethyl groups in BDM are sequentially oxidized. The dissociative protons are either adsorbed on PPy@ZIS composite or reduced by photoexcited electrons, which helps prevent charge carrier

recombination. As a result, the photoinduced charge carriers are efficiently separated, thereby prolonging the lifetime and enhancing the photocatalytic activity.

#### 4. Conclusions

In summary, ultrathin ZIS nanosheets were successfully decorated on PPy nanotubes to form hierarchical PPy@ZIS composite for simultaneous photocatalytic  $\text{H}_2$  evolution and selective BDM oxidation to PAD under visible light irradiation. The hierarchical 10%-PPy@ZIS composite shows the highest photocatalytic activity for water splitting to  $\text{H}_2$  ( $1428 \mu\text{mol g}^{-1} \text{h}^{-1}$ ) and selective oxidation of BDM to high value-added PAD ( $735 \mu\text{mol g}^{-1} \text{h}^{-1}$ ). The long-term (36 h) photocatalytic activity of 10%-PPy@ZIS show excellent stability and high efficiency of BDM oxidation conversion (89.5%) and PAD production selectivity (98.9%). In this work, the PPy nanotubes act as an electrons collector and trigger the photoexcited electrons directional migration, which may boost the  $\text{H}_2$  production from water, and the photoexcited holes on ZIS nanosheets can rapidly consume by BDM. The photocatalytic selective oxidation of BDM to PAD is the carbon-centered free radical process, and the S vacancies of PPy@ZIS composite are conducive to BDM selective oxidation. This work is expected to use both photoexcited electrons and holes for photoredox reactions, which can significantly improve the efficiency of solar-to-chemical and produce high value-added products.

#### CRediT authorship contribution statement

**Xinxin Peng:** Investigation, Conceptualization, Methodology, Writing – original draft, Visualization. **Junwei Li:** Formal analysis, Software, Visualization, Data curation. **Luocai Yi:** Investigation, Conceptualization, Validation. **Xi Liu:** Investigation, Characterization, Validation. **Junxiang Chen:** Formal analysis, Software, Visualization, Data curation. **Pingwei Cai:** Writing – review & editing. **Zhenhai Wen:** Supervision, Conceptualization, Writing – review & editing, Data curation, Resources, Funding acquisition.



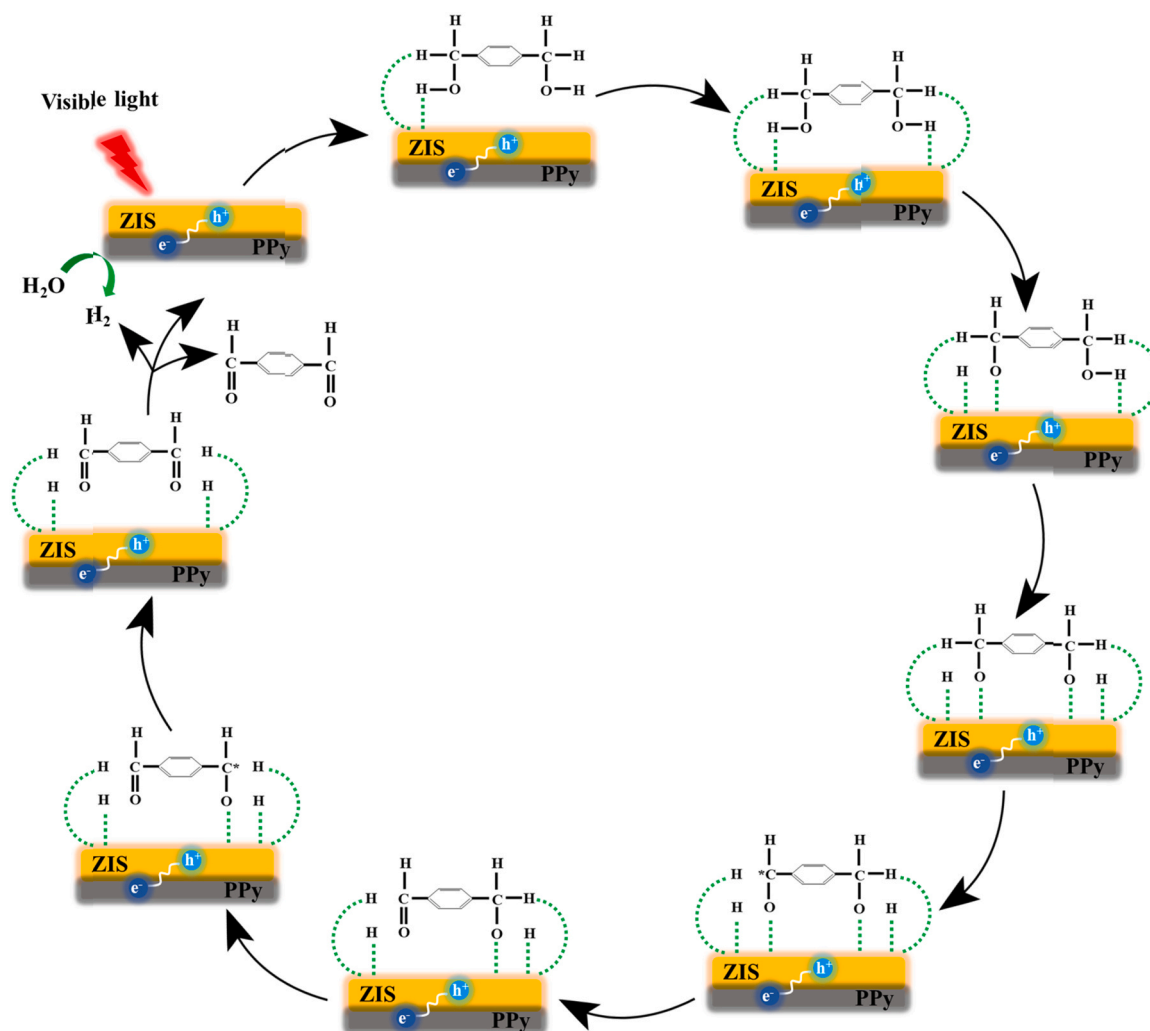


Fig. 6. Proposed reaction mechanism for coupling photocatalytic  $H_2$  evolution and BDM oxidation on PPy@ZIS composite under visible light illumination.

## Declaration of Competing Interest

The authors declare that they have no known competing financial interests or personal relationships that could have appeared to influence the work reported in this paper.

## Acknowledgements

This work was supported by the National Natural Science Foundation of China (Project No. 21875253), CAS-Commonwealth Scientific and Industrial Research Organization (CSIRO) Joint Research Projects (121835KYSB20200039), and Scientific Research and Equipment Development Project of CAS (YJKYYQ20190007).

## Appendix A. Supporting information

Supplementary data associated with this article can be found in the online version at [doi:10.1016/j.apcatb.2021.120737](https://doi.org/10.1016/j.apcatb.2021.120737).

## References

- [1] M.Z. Rahman, M.G. Kibria, C.B. Mullins, Metal-free photocatalysts for hydrogen evolution, *Chem. Soc. Rev.* 49 (2020) 1887–1931.
- [2] S. Ardo, D. Fernandez Rivas, M.A. Modestino, V. Schulze Greiving, F.F. Abdi, E. Alarcon Llado, V. Artero, K. Ayers, C. Battaglia, J.-P. Becker, D. Bederak, A. Berger, F. Buda, E. Chinello, B. Dam, V. Di Palma, T. Edvinsson, K. Fujii, H. Gardeniers, H. Geerlings, S.M.H. Hashemi, S. Haussener, F. Houle, J. Huskens, B. D. James, K. Konrad, A. Kudo, P.P. Kunturu, D. Lohse, B. Mei, E.L. Miller, G. F. Moore, J. Muller, K.L. Orchard, T.E. Rosser, F.H. Saadi, J.-W. Schütttauf, B. Seger, S.W. Sheehan, W.A. Smith, J. Spurgeon, M.H. Tang, R. van de Krol, P.C.K. Vesborg, P. Westerik, Pathways to electrochemical solar-hydrogen technologies, *Energy Environ. Sci.* 11 (2018) 2768–2783.
- [3] Q. Wang, K. Domen, Particulate photocatalysts for light-driven water splitting: Mechanisms, challenges, and design strategies, *Chem. Rev.* 120 (2019) 919–985.
- [4] T.H. Jeon, M.S. Koo, H. Kim, W. Choi, Dual-functional photocatalytic and photoelectrocatalytic systems for energy- and resource-recovering water treatment, *ACS Catal.* 8 (2018) 11542–11563.
- [5] B. Xia, Y. Zhang, B. Shi, J. Ran, K. Davey, S.Z. Qiao, Photocatalysts for hydrogen evolution coupled with production of value-added chemicals, *Small, Methods* 4 (2020), 2000063.
- [6] T. Banerjee, F. Podjaski, J. Kröger, B.P. Biswal, B.V. Lotsch, Polymer photocatalysts for solar-to-chemical energy conversion, *Nat. Rev. Mater.* 6 (2020) 168–190.
- [7] X. Deng, Z. Li, H. Garcia, Visible light induced organic transformations using Metal-organic-frameworks (MOFs), *Chemistry* 23 (2017) 11189–11209.
- [8] G. Laudadio, Y. Deng, K. v.d. Wal, D. Ravelli, M. Nuño, M. Fagnoni, D. Guthrie, Y. Sun, T. Noël, C(sp<sup>3</sup>)-H functionalizations of light hydrocarbons using decatungstate photocatalysis in flow, *Science* 369 (2020) 92–96, 92+.
- [9] J. Liu, Y. Zhang, Z. Huang, Z. Bai, Y. Gao, Photoelectrocatalytic oxidation of methane into methanol over ZnO nanowire arrays decorated with plasmonic Au nanoparticles, *Nano* 14 (2019), 1950017.
- [10] S. Gisbertz, S. Reischauer, B. Pieber, Overcoming limitations in dual photoredox/nickel-catalysed C–N cross-couplings due to catalyst deactivation, *Nat. Catal.* 3 (2020) 611–620.
- [11] N.A. Till, L. Tian, Z. Dong, G. Scholes, D.W.C. MacMillan, A mechanistic analysis of metallaphotoredox C–N coupling: photocatalysis initiates and perpetuates Ni(I)/Ni(III) coupling activity, *J. Am. Chem. Soc.* 142 (2020) 15830–15841.
- [12] Q. Zhang, X. Xiang, Y. Ge, C. Yang, B. Zhang, K. Deng, Selectivity enhancement in the g-C<sub>3</sub>N<sub>4</sub>-catalyzed conversion of glucose to gluconic acid and glucaric acid by modification of cobalt thiophenopyrazine, *J. Catal.* 388 (2020) 11–19.



- [13] T. Zhu, X. Ye, Q. Zhang, Z. Hui, X. Wang, S. Chen, Efficient utilization of photogenerated electrons and holes for photocatalytic redox reactions using visible light-driven Au/ZnIn<sub>2</sub>S<sub>4</sub> hybrid, *J. Hazard. Mater.* 367 (2019) 277–285.
- [14] S. Song, J. Qu, P. Han, M.J. Hulse, G. Zhang, Y. Wang, S. Wang, D. Chen, J. Lu, N. Yan, Visible-light-driven amino acids production from biomass-based feedstocks over ultrathin CdS nanosheets, *Nat. Commun.* 11 (2020) 4899.
- [15] D. Liu, J.C. Liu, W. Cai, J. Ma, H.B. Yang, H. Xiao, J. Li, Y. Xiong, Y. Huang, B. Liu, Selective photoelectrochemical oxidation of glycerol to high value-added dihydroxyacetone, *Nat. Commun.* 10 (2019) 1779.
- [16] W. Shang, Y. Li, H. Huang, F. Lai, M.B.J. Roeffaers, B. Weng, Synergistic redox reaction for value-added organic transformation via dual-functional photocatalytic systems, *ACS Catal.* 11 (2021) 4613–4632.
- [17] Q. Lin, Y.-H. Li, M.-Y. Qi, J.-Y. Li, Z.-R. Tang, M. Anpo, Y.M.A. Yamada, Y.-J. Xu, Photoredox dual reaction for selective alcohol oxidation and hydrogen evolution over nickel surface-modified ZnIn<sub>2</sub>S<sub>4</sub>, *Appl. Catal. B: Environ.* 271 (2020), 118946.
- [18] M. Zhou, Z. Chen, P. Yang, S. Wang, C. Huang, X. Wang, Hydrogen reduction treatment of boron carbon nitrides for photocatalytic selective oxidation of alcohols, *Appl. Catal. B: Environ.* 276 (2020), 118916.
- [19] Z. Sun, X. Yang, X.-F. Yu, L. Xia, Y. Peng, Z. Li, Y. Zhang, J. Cheng, K. Zhang, J. Yu, Surface oxygen vacancies of Pd/Bi<sub>2</sub>MoO<sub>6</sub>-x acts as “Electron Bridge” to promote photocatalytic selective oxidation of alcohol, *Appl. Catal. B: Environ.* 285 (2021), 119790.
- [20] G. Han, Y.H. Jin, R.A. Burgess, N.E. Dickenson, X.M. Cao, Y. Sun, Visible-light-driven valorization of biomass intermediates integrated with H<sub>2</sub> production catalyzed by ultrathin Ni/CdS nanosheets, *J. Am. Chem. Soc.* 139 (2017) 15584–15587.
- [21] H. Wang, Y. Song, J. Xiong, J. Bi, L. Li, Y. Yu, S. Liang, L. Wu, Highly selective oxidation of furfuryl alcohol over monolayer titanate nanosheet under visible light irradiation, *Appl. Catal. B-Environ.* 224 (2018) 394–403.
- [22] K. Targos, O.P. Williams, Z.K. Wickens, Unveiling potent photooxidation behavior of catalytic photoreductants, *J. Am. Chem. Soc.* 143 (2021) 4125–4132.
- [23] L. Zhong, B. Mao, M. Liu, M. Liu, Y. Sun, Y.-T. Song, Z.-M. Zhang, T.-B. Lu, Construction of hierarchical photocatalysts by growing ZnIn<sub>2</sub>S<sub>4</sub> nanosheets on Prussian blue analogue-derived bimetallic sulfides for solar co-production of H<sub>2</sub> and organic chemicals, *J. Energy Chem.* 54 (2021) 386–394.
- [24] F. Tian, R. Zhu, K. Song, M. Niu, F. Ouyang, G. Cao, The effects of hydrothermal temperature on the photocatalytic performance of ZnIn<sub>2</sub>S<sub>4</sub> for hydrogen generation under visible light irradiation, *Mater. Res. Bull.* 70 (2015) 645–650.
- [25] J. Zhao, X. Yan, N. Zhao, X. Li, B. Lu, X. Zhang, H. Yu, Cocatalyst designing: a binary noble-metal-free cocatalyst system consisting of ZnIn<sub>2</sub>S<sub>4</sub> and In(OH)<sub>3</sub> for efficient visible-light photocatalytic water splitting, *RSC Adv.* 8 (2018) 4979–4986.
- [26] J. Wang, S. Sun, R. Zhou, Y. Li, Z. He, H. Ding, D. Chen, W. Ao, A review: synthesis, modification and photocatalytic applications of ZnIn<sub>2</sub>S<sub>4</sub>, *J. Mater. Sci. Technol.* 78 (2021) 1–19.
- [27] B. Lin, H. Li, H. An, W. Hao, J. Wei, Y. Dai, C. Ma, G. Yang, Preparation of 2D/2D g-C<sub>3</sub>N<sub>4</sub> nanosheet@ZnIn<sub>2</sub>S<sub>4</sub> nanoleaf heterojunctions with well-designed high-speed charge transfer nanochannels towards high-efficiency photocatalytic hydrogen evolution, *Appl. Catal. B-Environ.* 220 (2018) 542–552.
- [28] X. Wang, X. Wang, J. Huang, S. Li, A. Meng, Z. Li, Interfacial chemical bond and internal electric field modulated Z-scheme Sv-ZnIn<sub>2</sub>S<sub>4</sub>/MoSe<sub>2</sub> photocatalyst for efficient hydrogen evolution, *Nat. Commun.* 12 (2021) 4112.
- [29] B. Gao, W. Chen, S. Dong, J. Liu, T. Liu, L. Wang, M. Sillanpää, Polypyrrole/ZnIn<sub>2</sub>S<sub>4</sub> composite photocatalyst for enhanced mineralization of chloramphenicol under visible light, *J. Photoch. Photobio. A* 349 (2017) 115–123.
- [30] Y. Li, S. Yan, X. Jia, J. Wu, J. Yang, C. Zhao, S. Wang, H. Song, X. Yang, Uncovering the origin of full-spectrum visible-light-responsive polypyrrole supramolecular photocatalysts, *Appl. Catal. B: Environ.* 287 (2021), 119926.
- [31] S. Wang, B.Y. Guan, X. Wang, X.W.D. Lou, Formation of hierarchical Co<sub>9</sub>S<sub>8</sub>@ZnIn<sub>2</sub>S<sub>4</sub> heterostructured cages as an efficient photocatalyst for hydrogen evolution, *J. Am. Chem. Soc.* 140 (2018) 15145–15148.
- [32] L. Shang, C. Zhou, T. Bian, H. Yu, L.-Z. Wu, C.-H. Tung, T. Zhang, Facile synthesis of hierarchical ZnIn<sub>2</sub>S<sub>4</sub> submicrospheres composed of ultrathin mesoporous nanosheets as a highly efficient visible-light-driven photocatalyst for H<sub>2</sub> production, *J. Mater. Chem. A* 1 (2013) 4552.
- [33] Y. Yang, L.C. Yin, Y. Gong, P. Niu, J.Q. Wang, L. Gu, X. Chen, G. Liu, L. Wang, H. M. Cheng, An unusual strong visible-light absorption band in red anatase TiO<sub>2</sub> photocatalyst induced by atomic hydrogen-occupied oxygen vacancies, *Adv. Mater.* 30 (2018), 1704479.
- [34] L. Yang, M. Lv, Y. Song, K. Yin, X. Wang, X. Cheng, K. Cao, S. Li, C. Wang, Y. Yao, W. Luo, Z. Zou, Porous Sn<sub>3</sub>O<sub>4</sub> nanosheets on PPy hollow rod with photo-induced electrons oriented migration for enhanced visible-light hydrogen production, *Appl. Catal. B: Environ.* 279 (2020), 119341.
- [35] X. Peng, L. Ye, Y. Ding, L. Yi, C. Zhang, Z. Wen, Nanohybrid photocatalysts with ZnIn<sub>2</sub>S<sub>4</sub> nanosheets encapsulated UiO-66 octahedral nanoparticles for visible-light-driven hydrogen generation, *Appl. Catal. B: Environ.* 260 (2020), 118152.
- [36] Y. Xiao, G. Tian, W. Li, Y. Xie, B. Jiang, C. Tian, D. Zhao, H. Fu, Molecule self-assembly synthesis of porous few-layer carbon nitride for highly efficient photoredox catalysis, *J. Am. Chem. Soc.* 141 (2019) 2508–2515.
- [37] X. Yuan, D. Floresyona, P.-H. Aubert, T.-T. Bui, S. Remita, S. Ghosh, F. Brisset, F. Goubard, H. Remita, Photocatalytic degradation of organic pollutant with polypyrrole nanostructures under UV and visible light, *Appl. Catal. B-Environ.* 242 (2019) 284–292.
- [38] Q. Zhou, Z. Zhang, J. Cai, B. Liu, Y. Zhang, X. Gong, X. Sui, A. Yu, L. Zhao, Z. Wang, Z. Chen, Template-guided synthesis of Co nanoparticles embedded in hollow nitrogen doped carbon tubes as a highly efficient catalyst for rechargeable Zn-air batteries, *Nano Energy* 71 (2020), 104592.
- [39] W. Xu, W. Gao, L. Meng, W. Tian, L. Li, Incorporation of sulfate anions and sulfur vacancies in ZnIn<sub>2</sub>S<sub>4</sub> photoanode for enhanced photoelectrochemical water splitting, *Adv. Energy Mater.* 11 (2021), 2101181.
- [40] S. Zhang, X. Liu, C. Liu, S. Luo, L. Wang, T. Cai, Y. Zeng, J. Yuan, W. Dong, Y. Pei, Y. Liu, MoS<sub>2</sub> quantum dot growth induced by S vacancies in a ZnIn<sub>2</sub>S<sub>4</sub> monolayer: Atomic-level heterostructure for photocatalytic hydrogen production, *ACS Nano* 12 (2018) 751–758.
- [41] J. Chen, F. Xin, H. Niu, C.-J. Mao, J.-M. Song, Photocatalytic reduction of CO<sub>2</sub> with methanol over Bi<sub>2</sub>S<sub>3</sub>-ZnIn<sub>2</sub>S<sub>4</sub> nanocomposites, *Mater. Lett.* 198 (2017) 1–3.
- [42] Y. Chen, G. Tian, Z. Ren, K. Pan, Y. Shi, J. Wang, H. Fu, Hierarchical core-shell carbon nanofiber@ZnIn<sub>2</sub>S<sub>4</sub> composites for enhanced hydrogen evolution performance, *ACS Appl. Mater. Interfaces* 6 (2014) 13841–13849.
- [43] X. Jing, N. Lu, J. Huang, P. Zhang, Z. Zhang, One-step hydrothermal synthesis of S-defect-controlled ZnIn<sub>2</sub>S<sub>4</sub> microflowers with improved kinetics process of charge-carriers for photocatalytic H<sub>2</sub> evolution, *J. Energy Chem.* 58 (2021) 397–407.
- [44] J. Pan, G. Zhang, Z. Guan, Q. Zhao, G. Li, J. Yang, Q. Li, Z. Zou, Anchoring Ni single atoms on sulfur-vacancy-enriched ZnIn<sub>2</sub>S<sub>4</sub> nanosheets for boosting photocatalytic hydrogen evolution, *J. Energy Chem.* 58 (2021) 408–414.
- [45] E. Zhang, Q. Zhu, J. Huang, J. Liu, G. Tan, C. Sun, T. Li, S. Liu, Y. Li, H. Wang, X. Wan, Z. Wen, F. Fan, J. Zhang, K. Ariga, Visually resolving the direct Z-scheme heterojunction in CdS@ZnIn<sub>2</sub>S<sub>4</sub> hollow cubes for photocatalytic evolution of H<sub>2</sub> and H<sub>2</sub>O<sub>2</sub> from pure water, *Appl. Catal. B: Environ.* 293 (2021), 120213.
- [46] X. Yuan, D. Dragoe, P. Beaunier, D.B. Uribe, L. Ramos, M.G. Méndez-Medrano, H. Remita, Polypyrrole nanostructures modified with mono- and bimetallic nanoparticles for photocatalytic H<sub>2</sub> generation, *J. Mater. Chem. A* 8 (2020) 268–277.
- [47] L. Sun, X. Huang, Y. Li, L. Deng, H. Mi, X. Ren, P. Zhang, Controlled synthesis and lithium storage performance of NiCo<sub>2</sub>O<sub>4</sub>/PPy composite materials, *J. Phys. Chem. Solids* 148 (2021), 109761.
- [48] D. Jiang, Covalent organic frameworks: an amazing chemistry platform for designing polymers, *Chem* 6 (2020) 2461–2483.
- [49] G. Zeng, H. Zeng, L. Niu, J. Chen, T. Song, P. Zhang, Y. Wu, X. Xiao, Y. Zhang, S. Huang, A promising alternative for sustainable and highly efficient solar-driven deuterium evolution at room temperature by photocatalytic D<sub>2</sub>O splitting, *ChemSusChem* 13 (2020) 2935–2939.
- [50] J. Lan, V.V. Rybkin, M. Iannuzzi, Ionization of water as an effect of quantum delocalization at aqueous electrode interfaces, *J. Phys. Chem. Lett.* 11 (2020) 3724–3730.
- [51] H. Fu, B. Wu, L. Zhang, B. Jiang, Q. Li, C. Tian, Y. Xie, W. Li, Ultrathin porous carbon nitride bundles with an adjustable energy band structure toward simultaneous solar photocatalytic water splitting and selective phenylcarbinol oxidation, *Angew. Chem. Int. Ed.* 60 (2021) 4815–4822.
- [52] A. Bosnjakovic, S. Schlick, Spin trapping by 5,5-dimethylpyrroline-N-oxide in fenton media in the presence of nafion perfluorinated membranes: limitations and potential, *J. Phys. Chem. B* 110 (2006) 10720–10728.
- [53] Z. Wang, W. Ma, C. Chen, H. Ji, J. Zhao, Probing paramagnetic species in titania-based heterogeneous photocatalysis by electron spin resonance (ESR) spectroscopy—a mini review, *Chem. Eng. J.* 170 (2011) 353–362.